A MOLECULAR DYNAMICS INVESTIGATION OF SIDE-CHAIN INFLUENCE ON THE FORMATION OF A8-35 AMPHIPOL PARTICLES

A THESIS
SUBMITTED TO THE FACULTY OF THE GRADUATE SCHOOL
OF THE UNIVERSITY OF MINNESOTA
BY

WILLIAM JOSEPH DRASLER II

IN PARTIAL FULFILLMENT OF THE REQUIREMENTS
FOR THE DEGREE OF
MASTER OF SCIENCE

DR. JONATHAN SACHS

JANUARY 2012

Acknowledgements

It is a pleasure to thank those that have helped to make this thesis possible. I would like to thank my advisor Dr. Jonathan Sachs for his support throughout my graduate research experience. I thank my colleagues Dr. Jason Perlmutter, and Dr. Christopher Valley for the privilege of collaborating with them. I thank Dr. Victor Barocas and Dr. Chun Wang for their insightful input and suggestions. Finally, I would like to thank the department of biomedical engineering for providing the resources necessary to make this research possible.

Dedication

I dedicate this thesis to my family and friends.

Abstract

We present all-atom molecular dynamics simulations of A8-35 amphipol, a polymer designed to stabilize the native conformation of membrane proteins in aqueous solution. These simulations were designed to reproduce the experimentally observed self-assembly of four A8-35 chains into a particle with an approximate molar mass of 40 kD as previously reported by Gohon et al. Comparison between the simulations and small angle neutron scattering confirms the nanometer scale structure of the particle. Using atomistic resolution, we have studied the polymers ability to form microdomains of like moieties, a feature with implications in the stabilization of membrane proteins. Using five distinct side-chain sequences, we observe different extents of side-chain self-association. An additional simulation describes the affect of a higher ionic concentration, which causes a dramatic reorganization of the particle, leading to increased side-chain self-association. Collectively, these simulations describe with atomistic detail the range of structures observed in a statistical polymerization, suggesting which features may be exploited for the improvement of membrane protein stabilization.

Table of Contents

Table of Contents

Acknowledgements..……...i

Dedication……...ii

Abstract…….iii

List of Tables…….……...…….……v

List of Figures……...…….……vi

Introduction

Amphipol Polymer……...1

Molecular Dynamics…….……...3

Methods

Parameterization……..……6

Simulation Setup……..……6

Small Angle Neutron Scattering…….…….....……8

Contrast Variation……...9

Results

Particle Assembly……...…12

Experimental verification through SANS……...……14

CMP analysis through SANS…….……15

Side-Chain Distribution and Water Content…….…….16

Discussion……...…….……...……..19

Conclusions and Future Directions…….…….……..24

Figures…….……..28

References…….43

Appendix……...46

List of Tables

Table 1. Number of TIP3 water residues and ions used in each particle simulation……31

Table 2. Radius of gyration at infinite contrast for each of the particle models……...38

Table A1. CHARMM parameters utilized for each of the particle simulations……...46

List of Figures

Figure 1. Molecular representation and schematic of the chemical structure of A8-35 amphipol……28

Figure 2. Previously parameterized model compound with chemical similarity…….....29

Figure 3. Diagram representation of the successful starting configuration used……...30

Figure 4. A graphical simplification that represents the side-chain ordering…….....32

Figure 5. The root mean square deviation (RMSD) plotted against simulation time ….……..…33

Figure 6. Equilibration of the radius of gyration for each particle over the course of the simulation……...34

Figure 7. A. Solution behavior of A8-35 particle as probed through SANS……...……..35

Figure 8. Rg^2 plotted against inverse of contrast for hapol amphipol particles……...…..…..……..36

Figure 9. Rg^2 plotted against inverse of contrast for dapol amphipol particles……...……..37

Figure 10. Representative snapshots taken after 50 ns of dynamics……..……...39

Figure 11. Water molecules present at the particle center vs. simulation time……..……...40

Figure 12. Average number of sodium ions bound to carbonyl oxygens ……..…41

Figure 13. Radial probability distribution of hydrophilic and hydrophobic side-chains ……...……..42

Introduction

Amphipol

Obtaining detailed structural information for membrane proteins is profoundly important for the development of future drugs and medical therapies but is a notoriously difficult task [1–3]. These membrane proteins are often composed of several subunits and are oriented across the lipid bilayer of a cell. Their orientation, associations, and structure are crucial to their activity in cellular functions [3–5]. Unlike soluble proteins, membrane proteins have both polar and non-polar groups exposed on their surface. This duality in nature causes them to rapidly aggregate and drop out of solution when placed in an aqueous environment. Classically, detergents have been used to solubilize these proteins by associating with their non-polar transmembrane region [3]. However, the dissociating nature of detergents rapidly distorts their structures into non-native configurations.

While the use of detergents aided a great deal of structural studies, their failure to stabilize functionally active, oligomeric states severely limits their efficacy in a majority of structural membrane protein studies [6]. Additionally, the micelle-forming nature of detergents requires that their concentration be kept above a critical concentration (CMC). To overcome these obstacles, a novel class of amphipathic polymers designated “amphipols” has been introduced and investigated as an alternative to detergents in protein structural investigations. Drawing from polysoap research, amphipols were constructed using polyacrylic acid (PAA), which has a highly flexible backbone free of conjugated bonds [6–8]. This flexibility allows the polymer to wrap easily around a tight circumference, such as a membrane protein. To confer the hydrophobicity required to

interface with the trans-membrane region of membrane proteins straight-chain alkyl groups were grafted on.

Several versions of this polymer were tested; the most effective version of this polymer was found to be one with an octylamine graft, which is the shortest side-chain capable of conferring micelle-forming properties in PAA [7]. The specific version has been termed A8-35, with the 'A' referring to the anionic PAA backbone, the 8 to the average backbone mass in kDa (~70 units), and the 35 to the percentage of free, negatively charged, ungrafted carboxylates [8]. 25% of the backbone is derivitized with octylamine to confer hydrophobicity, in order to stabilize the protein's hydrophobic transmembrane domain (see Figure 1). The remaining 40% is derivitized with isopropylamine to reduce the charge density along the backbone.

Amphipols strongly but non-permanently bind to the transmembrane region of membrane proteins and solubilize them while maintaining their active form. Unlike detergents, these amphipols perform this function in the absence of an appreciable concentration of free monomers [2,9]. The efficacy of amphipols has been experimentally shown through successful structural studies of several membrane proteins (for review see [2,6]). To successfully utilize amphipols for a wide range of membrane proteins, it is imperative that we understand how these amphipol particles stabilize membrane proteins, which requires an understanding of how the self-assembled structures of these polymers form [8].

Despite the polydispersity of the backbone PAA, these polymers self-assemble into well-defined particles with a narrow size distribution, an association number of 4,

and an observed mass of ~40 kD [8]. The unusually well defined association number found in these particles results from a lack of sufficient octyl chains present on a single polymer chain to display micelle-like polymer properties on their own. However, when associated into groupings of four, the number of octyl chains is within range to exhibit micelle-like properties [7].

It is thought that the self-assembly of these four amphipol chains is hydrophobically driven and is crucial for the stabilizing effect on membrane proteins and is an important property to examine. A8-35 assemblies have been characterized through several methods, including viscosity measurements, size exclusion chromatography, small-angle x-ray and neutron scattering, quasi-elastic light scattering and analytical centrifugation [8,10]. However, details of the molecular level structure remains unresolved. It is the intention of this research to provide the first step in understanding the molecular details of these amphipol particles through the use of atomistic molecular dynamics simulations.

Molecular dynamics

Molecular Dynamics (MD) simulation has proven a useful tool for studying the structure of soluble proteins, membrane proteins, and polymers. MD is the technique of modeling the configuration and motion of molecules through calculations of interaction energies using principles of classical physics. In the case of all-atom molecular dynamics, each atom in the system is considered explicitly. This approach models each atom as a sphere, with a parameterized radius, mass and partial charge localized to the center of the sphere. The potential energy of the system is computed by summing the energy of local

and non-local interaction terms. The simulation program CHARMM utilizes the terms shown in Equation 1.1 for the potential energy calculation [11,12].

$$U_{total} = \sum_{bonds} k_b(b - b_0)^2 + \sum_{angles} k_\theta(\theta - \theta_0)^2 + \sum_{dihedrals} k_\emptyset[1 + \cos(n\emptyset - \delta)]$$
$$+ \sum_{Urey-Bradley} k_{UB}(S - S_0)^2 + \sum_{Impropers} k_{IMP}(\varphi - \varphi_0)^2$$
$$+ \sum_{Nonbonded} \epsilon\left[\left(\frac{R_{min\ ij}}{r_{ij}}\right)^{12} - \left(\frac{R_{min\ ij}}{r_{ij}}\right)^{6}\right] + \frac{q_i q_j}{\epsilon_1 r_{ij}} \quad (1.1)$$

with k_b, k_θ, k_ϕ, k_{UB}, and k_{IMP} representing the bond, angle, dihedral, Urey-Bradley, and improper force constant b represents bond distance, θ is bond angle, ϕ is the dihedral angle, S is the Urey-Bradley distance, φ is the improper distance, ε is the Leonard-Jones constant, R_{min} is the minimum distance between two atoms, r_{ij} is the distance between a pair of non-bonded atom, and q_i and q_j are the charges on a pair of atoms [12]. The parameters for Equation 1.1 are developed through direct comparison to quantum mechanical calculations [11,12].

The concept of molecular dynamics is relatively simple; Newton's equation of motion reveals that the derivative of potential energy with respect to position equals force. Therefore, by numerically integrating the gradient force field equation over discrete time intervals the vector forces acting on each molecule are found and are used to predict motion.

Initial velocities are pseudo-randomly generated so that the average kinetic energy $\langle E_k \rangle$ is equal to the value predicted for an equilibrated system by the equipartition

theorem. This theorem indicates that the average kinetic energy depends on the degrees of freedom, a constant, and the target temperature of the system.

$$\langle E_k \rangle = \frac{1}{2}\langle \sum_{i=1}^{3N} m_i v_i^2 \rangle = 3N \frac{k_B T}{2} \quad (1.2)$$

The calculation of $\langle E_k \rangle$ is shown in Equation 1.2 as the sum of the individual kinetic energies. By integrating the equations of motion with these initial velocities along with starting configurations allows us to find the resulting velocities and positions for each atom after each time step (which is typically 2 femtoseconds) [13].

Using MD we are able to model the structure and dynamics of an A8-35 assembly with atomistic detail. Previous experiments have been limited to an averaged view of the many different side-chain sequences formed by the statistical polymerization. By performing separate MD simulations with varied side-chain sequences, we are able to understand more about the structures of individual amphipol particles as a function of the chemical character of the amphipol side-chains. These simulations allow us to investigate how differences in side-chain sequence lead to distinct behaviors. In this way MD allows us to extend observations from experiments and investigate small-length scale phenomena that dictate their behavior. These results provide insight into amphipol structure and suggest new mechanisms for how they stabilize membrane proteins.

Methods

Parameterization

For areas where their chemical nature was identical, parameters for each amphipol residue were taken from N-methyl-2-ethyl butanamide (shown in Figure 2) which was previously parameterized in the CHARMM22 force field [12]. The angle extending from the carbonyl carbon to the first side-chain carbon differs from this analog as a result of the influence of the octylamine chain. The parameter for this bond was optimized by matching the normal modes to a quantum mechanical model. A complete set of the parameters used in these simulations is listed in Table A1.

Simulation Setup

Each polymer chain configuration was built using the CHARMM molecular mechanics package [11], with four polymer chains consisting of 89 units each, with charges balanced by the addition of sodium ions and solvated in a cubic box of TIP3 modeled water; the number of waters an ions included in each system is shown in Table 1[14]. The size of the solvation box was chosen so self-interaction through the periodic boundaries was avoided. Each simulation was run using the NAMD molecular dynamics package [15], using an approximately constant number of atoms (~70,000 atoms), constant pressure, and constant temperature, to form NPT ensembles. The temperature in each simulation was set to 303 K. A cut-off of 10 Å was used for Van der Waals interactions, and particle mesh Ewald summation was used for long range electrostatic interactions. The time step used was 2 fs, and all bonds involving hydrogen were fixed using the SHAKE algorithm. The molecules were visualized with VMD [16].

Since the explicit particle structure is currently unknown, an artificial starting configuration was developed. Several different 4-chain starting configurations were generated, and the particles that resulted after steepest decent minimization and ~10 ns dynamics were judged based on their cohesiveness and shape. One starting configuration attempted was formed by wrapping polymer chains successively around the latitudinal lines of a sphere. MD simulation indicated that this configuration caused the four chains to form an overly cylindrical shape with a radius of gyration significantly above what has been seen in experiment. Another attempted configuration was formed by placing four vacuum minimized globular chains adjacent to each other; this configuration did not have enough inter-chain interactions to form a coherent particle over the simulated length-scale (45 ns). We recognized that starting from a totally random organization and observing the formation of the particle was the ideal approach, but computational power limited us to using a "hand-built" approach for all-atom simulations. Our subsequent studies using a coarse-grained force-field allowed for the formation of particles from non-interacting chains[17]. Here, the starting configuration that was judged to best form a coherent spheroidal particle was generated as shown in Figure 3. With each of the four amphipol chains oriented as in-plane circles sequentially increasing in radius and rotated about a single axis.

Using this as a starting configuration, 50 ns simulations were run for several particle sequences. These sequences were chosen to encompass the range of possible sequences found from a statistical polymerization. Figure 4 illustrates these sequences graphically. Three configurations with randomized side-chains were generated using a

pseudo-random sequence generator with constraints requiring the residues to be proportioned as 35:25:40% for ungrafted:octylamine:isopropylamine; these chains are called Random 1-3. A 'Block' configuration was designed to have a maximal tendency to micellerize hydrophobic side groups; this chain has all of the octylamine groups sequential along the center of the chain. A 'Homogenous,' chain was also selected to explore a chain with limited micelle-forming ability. This chain has a roughly regular repeat unit of ungrafted-octylamine-isopropylamine. The Random 1 + 100mM NaCl configuration was generated with identical side-chain distribution and starting configuration as that of the Random 1 configuration, with additional ions added to bring the final concentration up 100mM NaCl.

Small Angle Neutron Scattering

Small-angle neutron scattering (SANS) is a technique for structural investigation in which electromagnetic radiation with a wavelength of 2-4 Å is used. The resulting scattered intensity is recorded over a range of scattering angles and contains structural information of the sample. In the case of solution scattering, these intensities are averaged over all orientations. Therefore, the structure of the sample cannot be solved uniquely but certain details of the structure are still accessible. CRYSON, a derivative of the CRYSOL program, was utilized to simulate small-angle neutron scattering (SANS) profiles from the atomic coordinates of each amphipol system [18]. To compare to the experimental work of Gohon et al.[8,10], SANS profiles were calculated for two versions of each particle, one with normal hydrogens bonded to the hydrocarbon side-chains (termed 'hapol') and the second, with deuterium in place of hydrogen on the octylamine and

isopropylamine side-chains (termed ‘dapol’).The simulated SANS intensities of the particle simulation with solvent background subtracted are computed for each frame of the trajectory after the initial 20 ns equilibration period. The simulated scattering intensities are on a relative scale and no normalization is required [18].

The radius of gyration (R_G) is a measure of the distribution of polymer with respect to its center of mass. The R_G is found from simulated SANS by utilizing the Guinier approximation. This simplification approximates scattering intensities using the first terms of a Maclaurin expansion. As the form of Equation 1.3 suggests, the scattered intensity is linear when plotted against Q^2 and R_G is extracted from the slope of this plot in the low Q region.

$$\ln I(Q) = \ln I(0) - \frac{Q^2 R_g^{\,2}}{3} \tag{1.3}$$

Contrast Variation

The net scattering in solution depends on the squared difference in scattering length-density between the solvent and the particle [19]. For neutron scattering, the scattering length of the solvent may be altered by changing the ratio of ^2H_2O to H_2O [20,21]. Changing the solvent scattering length alters the contrast (ρ) between the particle and solvent [21–23]. At high contrast the particle appears homogeneous and only the overall shape is visible. Since the particle is not entirely homogeneous, different portions of the particle have different average scattering lengths. As the contrast is lowered, the internal

structure of the particle influences the scattering as well; this allows the internal structure of the particle to be examined [21].

As noted from Stuhrmann et al [21] the square root of zero angle scattering is proportional to contrast (ρ) and the volume inaccessible from solvent (V_c); this is shown in Equation 1.4 [21,24].

$$\sqrt[2]{I(0)} = \rho V_c. \tag{1.4}$$

This equation suggests that plotting the square root of zero-angle scattering intensity against $^2H_2O/H_2O$ solvent fraction (which alters ρ) will produce a linear trend. This trend is easily interpolated to revels the $^2H_2O/H_2O$ solvent fraction where the solution scattering matches the average scattering from the particle, known as the contrast match point. Equation 1.5 is utilized to calculate the solvent-exclusion volume of the particles, which then allows the contrast value at each $^2H_2O/H_2O$ concentration to be found by solving Equation 1.4 for contrast.

$$V_c = \frac{2\pi^2}{Q_0}, \tag{1.5}$$

with

$$Q_0 = \int_0^\infty \frac{I(s)}{I(0)} s^2 ds. \tag{1.6}$$

Where I(s) is the scattering intensity at a given scattering vector s, with $|s| = 2|\sin\theta|/\lambda$.

Because of inhomogeneities inside of the particle, the apparent radius of gyration of the particle is a function of contrast. When R_G^2 is plotted against the inverse contrast, the parabolic dependence of R_G^2 on 1/ρ emerges; this trend is shown in Equation 1.7 [20,21].

$$R_G^2 = R_C^2 + \frac{\alpha}{\rho} - \frac{\beta}{\rho^2} \quad (1.7)$$

The intersection of this curve with the ordinate gives the theoretical radius of gyration at infinite contrast (R_c). The alpha value, found from the slope at this intercept, indicates how scattering density varies with radial position. A positive alpha value indicates that the core has a higher scattering density, while a negative value indicates that the perimeter has a higher scattering density. The beta value is a measure of how the apparent center of mass displaces as contrast changes.

Results

Particle Assembly

The first result of this study is a stable structure of the A8-35 amphipol particle from a generated configuration. Since there was no experimentally determined, atomistic-resolution structure, we designed several possible starting configurations. However, only the starting configuration consisting of the four polymer chains arranged into concentric rings resulted in a successfully coalesced particle with spheroid geometry and appreciable side-chain reorganization. Other starting configurations either resulted in elongated structures of nearly cylindrical geometry, or did not have enough interactions to remain cohesive, and separated into individual globular chains. The relaxation of these polymers into cohesive particles within nanoseconds suggests that the selected starting configuration relaxes into an equilibrated structure and was useful for analysis of polymer side-chain behavior.

To quantitatively analyze the degree of equilibration and reorganization, the root mean squared deviation (RMSD) of the polyacrylate backbone was measured, as presented as Figure 5. Each sequence leads to particles which approach an equilibrium deviation of between 3 and 3.5 nm during the initial 20 ns of simulation. This indicates that this simulation timescale is appropriate to allow for sufficient relaxation of the polyacrylate backbone and reorganization of the side-chains inside of these particles. Block and Random 2 show larger deviations, while the Random 1 + 100mM NaCl particle shows lower deviation from the starting structure.

A similar pattern is observed in the radius of gyration, presented as Figure 6. Figure 6A shows the radius of gyration and its equilibration during 50 ns of simulation. Based on the radius of gyration and RMSD, we conclude that the particles have equilibrated after 20 ns; further analysis utilizes time-points after this cutoff. Inlaid images from Figure 6A illustrate the dynamic shape of these particles. These snapshots of the Random 1 particle are selected to convey the differences in sphericity that the particle assumes during the production portion of the dynamics. This illustrates the particles' dynamic ability to reversibly transform from more elongated ellipsoid structures to more spherical configurations. Figure 6B quantifies the average radius of gyration for each of the differently sequenced particles. Though each particle has the same total composition, the differences in sequence lead to difference in shape, as indicated by the radius of gyration. The Block and Random 2 sequences reorganize into slightly larger particles, with equilibrated average values of 2.59 nm. The smallest radius of gyration is found in the Random1 simulation run with 100mM NaCl which has an average value of 2.28 nm. This is a substantial decrease from the Random 1 simulation with only counter ions, which has an average value of 2.39 nm. Figure 6C illustrates how the differences in radius of gyration are caused by side-chain distribution. The Random 1 configuration has a relatively even distribution of side-chains throughout the molecule leading to a relatively compact particle; the backbone is effectively tethered to a hydrophobic core region by the octylamine grafts. In contrast, the Block configured particle has a near complete segregation of chemical groups, allowing the polar groups, along with that region of the backbone, to extend into solution, which results in an increase in the radius

of gyration. The radius of gyration values found here agree well with the experimental value (~2.3 nm) reported by Gohon [8].

Experimental verification through SANS

Comparison to experimental results is essential to validate any simulation study. Here, we have calculated the simulated small-angle neutron scattering (SSANS) from each simulation, and compared these results to the experimental SANS profiles reported in Gohon et al.[8]. This comparison is shown in Figure 7A [8]. The region of interest for particles of this size is $0.0015Å^{-2} < Q^2 < 1.6\ Å^{-2}$, while experimental scattering at lower values in inverse space is due to less prevalent, larger aggregates [8]. As can be seen in Figure 7A, the SANS calculated from the simulated particles is in agreement with the general shape and size reported in the experiments of Gohon [8]. This suggests that the structures we sample in this simulation are representative of the predominant size of amphipol particles seen in laboratory. The larger species which dominate the scattering at lower Q^2 values are absent in the simulation, and thus the SSANS profiles remains linear while the experimental SANS profile sees larger values. As expected from atomic coordinate calculations, the differences in particle sequence lead to slight differences in low Q scattering, indicating differences in macroscopic size. Additionally, differences in the mid-Q SANS profiles indicate differences in the microstructure inside the particle. All of the profiles match the experiment fairly well at ($Q^2 \sim 0.0015Å^{-2}$); the block and Random 2 are further from the experimental profile at higher Q than the other sequences.

In order to validate the simulated SANS from the simulations, we compare the radius of gyration extrapolated from the SANS to the radius of gyration calculated directly from the atomic coordinates. As Figure 7B shows, they lead to nearly identical values, except in the case with higher salt concentration. While SANS is useful for comparison of the particle size to experiment, because experiments were done with solution scattering, the curves are not unique to a structure and the atomic structure cannot be determined. Using molecular dynamics, we can observe in greater detail the molecular level interactions that lead to the differences between these particles.

CMP analysis through SANS

By varying the $^2H_2O/H_2O$ ratio, the point where average scattering length density of the particle matches that of the solution. Figure A1 and A2 show zero-angle scattering intensity plotted against $^2H_2O/H_2O$ fraction for hapol and dapol respectively. The contrast match point for hapol and dapol particles is 0.247±0.003 and 0.947±0.003 respectively. The match points for each particle are summarized in Table 1. These values differ slightly relative to the 0.224 and 0.910 values reported by Gohon [8,10]. These differences likely result from chemical differences in the experimental system caused by side-reactions in amphipol synthesis; most experiments to date have reported the presence of side-reactions [8,10].

Varying the contrast between particle and solution changes the apparent radius of gyration [25]. The apparent radius of gyration squared is plotted against inverse contrast for hapol and dapol in Figure 8 and 9. The intercept of these plots with the ordinate gives the radius of gyration at infinite contrast (R_c). These values are tabulated for hapol and dapol

in Table 1. Additionally, fitting this curve to a second order polynomial allows us to extract the α and β parameters from Equation 1.7. These parameters are shown in Table 1 for hapol and dapol.

Side-Chain Distribution and Water Content

Our simulations reveal that the major structural difference between particles with varied side-chain configurations is their ability to sequester hydrophobic side-chains and exclude water. Figure 10A is a snapshot of the Random 1 particle, which has groups of associated hydrophobic side-chains (shown in orange) distributed throughout the particle but maintains a core region that is accessible to water. This behavior is also seen in Random 3 and the Homogeneous sequences. Random 2, as illustrated in Figure 10B, as well as Block and the Random 1 + 100mM NaCl, all sequester sufficient hydrophobic groups in the particle center so that there is no void left to be occupied by water. In these particles, the octylamine groups cross the central region of the particle, effectively connecting opposing octylamine grafts, creating hydrophobic microdomains. All of the particles start without water in the center, however, over the course of the simulations water is able to enter and leave the particle core, as illustrated for the randomly sequenced particles in Figure 11A. This demonstrates that the water content is not determined by the starting configuration, and rather is a dynamic property determined by the structure, which is in turn dependent on the sequence. Figure 11B presents the time-average water radial density for representative systems. The Random 2 and Random 1 + 100mM NaCl are shown as representative of particles that exclude water (the Block

particle has a similar behavior). The water density is near zero in the particles center of mass, and gradually rises to the bulk water density at about ~3 nm from the particle center of mass. In contrast, the Random 1 and Random 3 particles are shown as representative of those particles which allow water penetration (the Homogenous particle has a similar behavior). In particular, the Random 1 structure contains a near bulk amount of water in the particle core.

Figure 13 shows the time-average radial distribution of water and side-chains in each particle. Using these data, we can attempt to correlate the presence or absence of water with the organization of the particle side-chains. Those particles that exclude water from the particle core are those which are able to segregate their hydrophobic side-chains into the particle center. In particular, in the Random 2 and Random 1 + 100 mM NaCl systems, we see a high concentration of octylamine at low radial values. Octylamine is known to have sufficient alkyl tail length to form micelle-like structures [7], and in these particles we observe several interdigitating octylamine side-chains, which prevent waters from residing in this location. In contrast, those particles that have water in the particle center do not show maximal densities of octylamine in the particle center, though the Homogenous particle does have some density near the particle center.

For those particles which do contain water in their interior, we might expect an enrichment of ungrafted units at their center of mass. This appears to be true for the Random 1 polymer, while not the case for Random 3 and Homogenous. This suggests that those polymers which are most able to segregate their hydrophobic side-chains prevent water penetration, while those polymers which are unable to segregate their

hydrophobic chains have a notable density of water in their interior. The Homogenous sequence is the one designed to exhibit the least amount of segregation, and therefore necessarily has some density of octylamine near the particle center, is unable to prevent the penetration of water.

Figure 13 shows the dramatic rearrangement the Random 1 sequence undergoes upon an increase of NaCl concentration to 100 mM. At the low salt concentration, there is a maximal amount of ungrafted side-chain and water in the particle center. The addition of more ions leads to octylamine being enriched in the particle center, while water is excluded and the ungrafted groups are moved towards the particle surface. This effect is likely the result of the increased electrostatic force that attracts the charged carbonyl oxygens toward the bulk solvent. The migration of these oxygen ions to the surface of the particle leaves a void that the octylamine grafts have entropic inclination to fill [26]. This increased drive causes these rearrangements to occur on a shorter time-scale.

Discussion

A deficiency in the understanding of the internal structure of hydrophobically grafted polyelectrolyte polymers has prompted numerous solution characterization studies [8,10,27]. Prior experiments (such as size exclusion chromatography (SEC) and viscosity measurement) began with a focus on macroscopic particle size and degree of association, but as a result of the detail required to utilize these particles in biophysical application, changed focus to the supramolecular level, with SANS used as the lowest length-scale probe [8,10]. We further the interpretation of these studies through connection between experiment and our all-atom models. We compared our simulated particles to experiments at this length-scale by matching the slope of the simulated SANS profiles at low Q to the previously published neutron scattering data [8]. The agreement with the size data from prior experiment validates our simulations and allows us to direct our attention to details of the low length-scale phenomena, which are currently only accessible through molecular dynamics simulation. The particles we designed encompass a range of configurations of side-chains, some with spacing between residues likely typical of those in experiment (e.g. Rand 1-3), others that are highly unlikely extreme cases that nevertheless provide insight into the types of interactions that exist in the particles (e.g. Block). Despite the constant number of alkyl tails present in each particle, we see markedly different size, internal structure, and water content in our particles. The evaluation of our parameter space gives insight into which molecular level details cause differences in the overall particle.

Differences in the distribution of side-chains shown in Figure 13 suggest that the sequencing of side-chains alters the degree to which like-natured moieties localize and form micelle-like microdomains. In order to observe the full range of possible behaviors in a statistical polymerization, we have included two extreme examples, the Block and Homogeneous configuration. By examining variations between these cases and the randomized configurations, we gain insight into how the density of octylamine chain groupings alters the internal organization of the resulting particle. The Homogeneous configuration has the most restrictive backbone constraints; and is correspondingly least able to segregate its side-chains according to chemical character. The degree of block-like nature impacts the methods of molecular association. The Block configuration has the fewest backbone imposed restrictions; its side-chains rearrange to form micelle-like structures with a water excluding core of hydrophobic groups. This finding is in agreement with particles seen in solution (the presence of water in the center would decrease the scattering density in this region, which was not seen in contrast match point SANS analysis from Gohon et al.[6,8].

The degree of block-like groupings of side-chain nature affects the intra-particle chain association behavior. In a statistical polymerization, it is probable that there will be small block-like groupings of octylamine along the polymer backbone. Variations in the side-chain sequence between the Random 1-3 configurations encompass these differences, which cause differences in the particle properties. Random 1 and 3 follow a trend, with a center region containing water without a high density of octylamines in this region. Random 2 is able to span the particle center in a micelle-like fashion, with a peak

of hydrophobic groups continuous across the particle center which effectively excludes water.

In agreement with what is expected from experiment, the configuration with an increased ion concentration directs particle assembly into a more compact particle. A partial contribution to this effect is the cross-linking effect that results from multiple negatively charged oxygens associated with a single sodium ion. Additionally, the elevated ion concentration screens the electrostatic charge that would otherwise repulse the polymer chains, allowing a defined hydrophobic core to develop, with exclusion of water. The large disparity in observed internal organization from the Random 1 without sodium strongly suggests that the alteration of the sodium parameter enables the particle to overcome predetermined direction imparted by starting configuration and be observed in the equilibrated particle.

We extend upon prior analysis by showing particles that closely match low length-scale data and expound on details of phenomena in detail that is not accessible to experiment. The atomistic characterization of these particles explicitly shows how the arrangement of alkyl tails along the backbone dictates their spatial organization in an equilibrated particle and how this determines overall particle size and properties. Through molecular dynamics simulation, we have probed a parameter space unavailable to the experimental world to illustrate how the properties the make up the polymer determine the overall particle. Control over these phenomena is important as we continue to bridge the gap in understanding from experiment to the atomic level of these polymers to further understand their unique interactions with membrane proteins.

These interactions are of much interest as they are responsible for stabilizing the protein structure in solution. It has been previously established that these interactions take place exclusively in the hydrophobic region of the MP. It has also been shown that more homogenous MP-amphipol particles form when an excess amphipol is added and the remaining polymer washed away. This suggests that the protein is effectively selecting the best collection of amphipol chains that solubilize its hydrophobic region. By examining these interactions through molecular dynamics, we can effectively screen a set of amphipols of varying length and composition and evaluate how well they isolate the hydrophobic region of the MP. In this way, we could utilize our work to develop a more effective amphipol.

Ion discussion

It is commonly accepted that for hydrophobically modified polymers, such as A8-35, an increase in ionic strength leads to an increase in hydrophobic association [28]. In order to investigate this phenomena we have simulated the Random 1 sequence at both a lower and higher ionic concentration. As has already been demonstrated, raising the ionic concentration to 100mM NaCl causes a significant rearrangement of the particle structure, which is described in Figure 13 and which leads to an increase in compactness as measured by the radius of gyration (Figure 6), a change in the SANS profile (Figure 7), and causes the polymer to exclude water from its interior (Figure 11). In order to describe why this occurs, we first quantify the extent to which each particle interacts with salt ions (Figure 12). For the particles with only counter-ions present, the block configuration has the largest number of ions bound, while Random 2 and Homogenous

have the least. In the Block particle, the ungrafted groups are most separated from the hydrophobic region and are accessible in solution, whereas in the Homogenous particle, the ungrafted groups are maximally interspaced between the hydrophobic particles, making the ungrafted side-chains less available to ions. The larger values for Random 1 and Random 3 suggest that the ungrafted side-chains are more able to find a solvent exposed surface, than in the Random 2 sequence. This may be due to the fact that Random 2 excludes water from the particle center, while in the Random 1 and Random 3 particles, this interior water provides additional surface for polymer-ion interaction.

Compared to the Random 1 particle with only counter-ions, the particle with 100 mM NaCl shows a substantial increase in particle-ion interaction. This increased interaction is the result of a structural rearrangement that is triggered by the increased ionic concentration. Figure 13 shows that the system with additional salt undergoes a substantial structural rearrangement. In particular, the polar side-chain density is lowered in the particle center and increased at higher radial values. This suggests that the presence of ions in solution “pulls” the polar groups towards the surface of the particle, causing the observed increase in ion association, as well as the other observed structural changes.

Conclusions and Future Directions

Amphipol polymers have been shown to stabilize MP's in solution; a process that involves complex interactions. These polymers bind to MP with sufficient tenacity to maintain contact in low concentrations and are gentle enough that they do not disrupt critical intramolecular MP interactions. The length and time scale of these association interactions have made accurate examination of these associations and stabilizing mechanisms difficult to analyze. Additionally, the polydispersity of the backbone and statistical derivitization of the grafted side-chains further obscure exactly which synthesized chain lengths and side-chain organizations are involved in these interactions.

A fundamental understanding of the solution behaviors of the pure amphipol particle system is crucial. For efficient use, a thorough characterization of the amphipol system is necessary. The simulations and analyses performed in this thesis characterize the intraparticle amphipol side-chain behaviors and describe how the ordering of the side chain affects the overall size of the particle. We correlated micellization and interdigitation particle behaviors to the ordering of hydrophobic side-chain groups along the polymer backbone. Additionally, we quantified the side-chain and water distributions inside of the particle.

Experimentally, these behaviors are of fundamental importance; they control the size, shape and compactness of the pure amphipol particle, which is the form introduced to MP. In solution, amphipols undergo two selection processes. The initial selection occurs when between amphipol chains as the polymers self-associate into particles

containing approximately four chains. To form a coherent particle, a critical number of octyl chains are required. Therefore chains with statistically fewer octylamines combine with chains with statistically elevated numbers in order to form monodisperse particles. In this way, the particle formation step involves binding complement chains, which provides an internal selection that averages out length and side-chain disparity. The second selection process occurs when these pure amphipol particles are introduced to an MP. Amphipol particles temporarily fuse and the MP effectively chooses chains that best bind to its transmembrane region. This selection (though not yet observed) is evidenced by the appreciably better MP stabilization that occurs when excess amphipol is initially added; since only under these conditions is the MP exposed to a large enough pool that it is able to select the best candidate.

The differences amongst the particles simulated in this thesis indicate that the statistical derivitization of the polymer backbone causes significant variations in the resulting particles. And as a result of the selection processes mentioned, it is apparent that certain chains bind MP more strongly than others. These simulations provide the framework to further examine which chain configurations provide the greatest advantage by examining which bind most strongly and how these interactions occur. This will more accurately show which chains are binding MP experimentally and which are present to assist in formation of pure amphipol particles. These future simulations will also give insight into which chain configuration provides the best balance of binding affinity to stabilization.

The insight provided from these simulations may be further developed to describe the optimal chain-length and side-chain organization. By generating a superior homogenous amphipol, we would effectively eliminate chain and MP selections, which would enhance the predictability and efficacy of the amphipol system. Rather than let the MP select the chains that best bind, we will engineer the chain that best stabilizes. Additionally, since each chain would be optimized, there would be no need to add excess polymer and the required concentrations of amphipol would be lower. This system would give better overall stabilization and with the number of octylamines optimized, would not require the addition of free lipid to supplement the chains and make the particles homogeneous.

These simulations illuminate previously unexplored details of the amphipol system. The features of the system at this length scale enhance the understanding of this critical system. These simulations have been extended in subsequent coarse-grained work to include de-novo particle assembly. These simulations may be further extended to investigate MP-amphipol fusing, attachment of MP-amphipol complexes to surfaces, and interactions of amphipol with lipid bilayers. These future studies may be connected to energetic experiments using measurements made through ITC and structural measurements through EM and NMR. Once the fusing and binding mechanisms are adequately characterized, steered MD simulations may prove useful to investigate the kinetics of Apol bound MP conformation changes in response to ligand binding, which may be connected to experimental data (which currently exists for Bacteriorhodopsin) to further validate the accuracy of amphipol stabilization. In these ways, the work of this

thesis advances the understanding of the amphipol polymer and raises interesting questions that will lead to more effective use and far-reaching applications of this polymer.

Figures

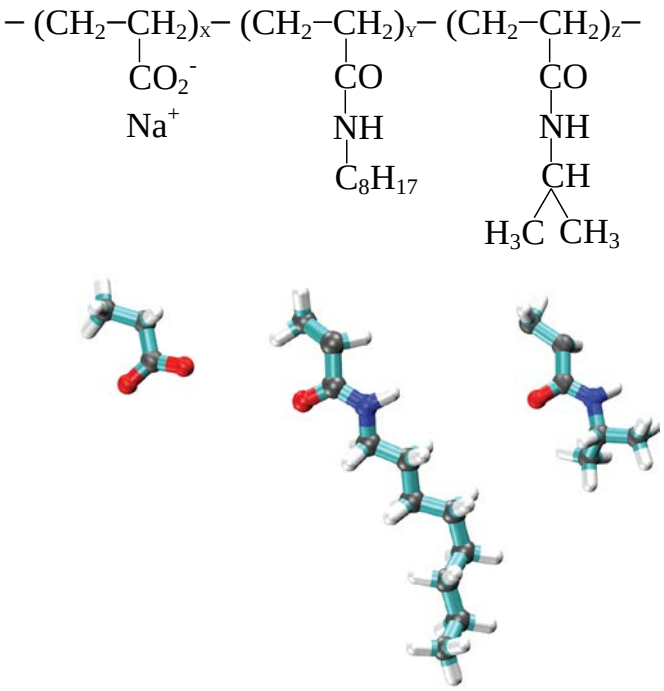

Figure 1. Molecular representation and schematic of the chemical structure of A8-35 amphipol, with residue proporitions (X, Y, and Z) having values of 35, 25, and 40% respectively. The carbons are represented in light grey, the Oxygens in red, the Nitogens in blue, and Hydrogens in white. Schematic representation of amphipol adapted from Gohon et al (8).

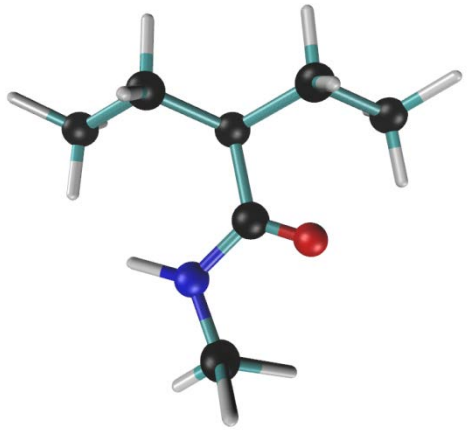

Figure 2. Previously parameterized (2-eththyl-N-methyl butanamide) model compound with chemical similarity to the A8-35 amphipol residues. Carbon backbone is shown in black, with red representing oxygen, blue representing nitrogen and white representing hydrogen [12].

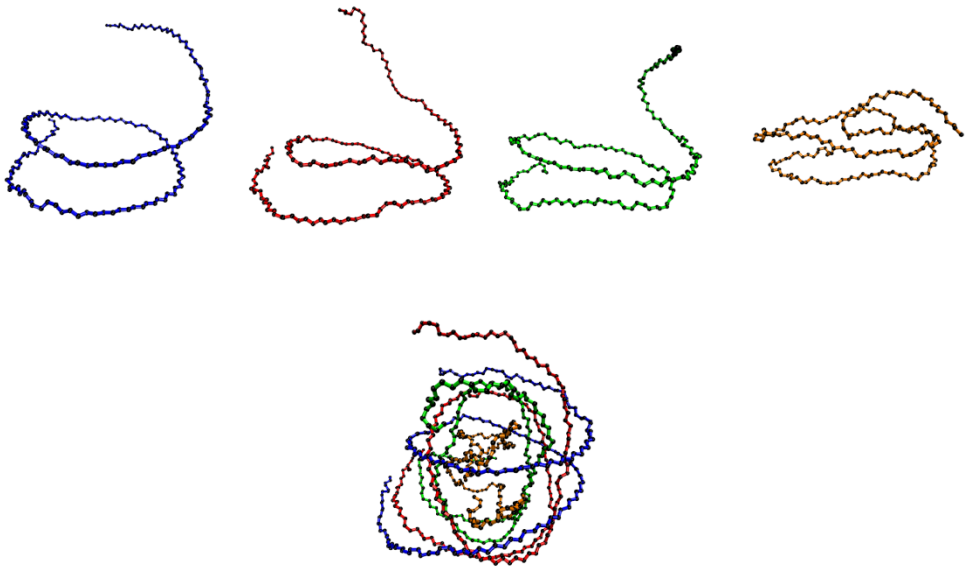

Figure 3. Diagram representation of the successful starting configuration used for each particle simulation. Each of the four chains has a sequentially decreasing diameter. Each of these chains was rotated and placed in sequential order from smallest to largest. Side-chains have been omitted from this figure and color is added to the backbone chain for clarity.

Table 1. Number of TIP3 water residues and ions included in each particle simulation.

	Water Molecules	Sodium Ions	Chloride Ions
Random 1	21644	124	0
Random 2	18780	124	0
Random 3	18805	124	0
Homogeneous	21494	124	0
Block	21586	124	0
Random 1 + 100mM NaCl	21619	163	39

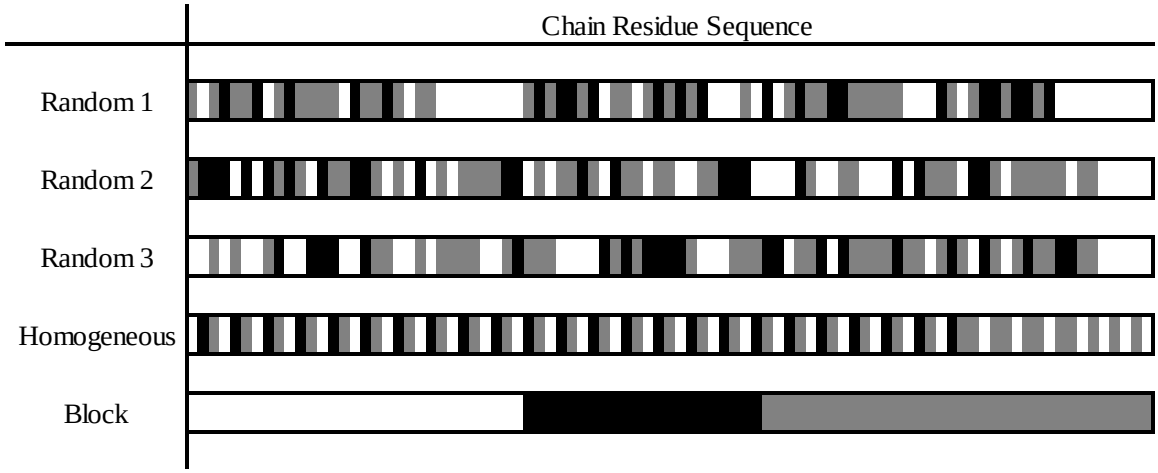

Figure 4. A graphically simplified representation of the side-chain ordering along the polyacrylate backbone for each of the simulations performed. Solid white represents an ungrafted residue, black represents an octylamine grafted residue, and grayed represents an isopropylamine grafted residue. Each particle contains four polymer chains of the listed sequence. The Random 1 + 100mM NaCl simulation is omitted since it has the same side-chain sequence as the Random 1 configuration.

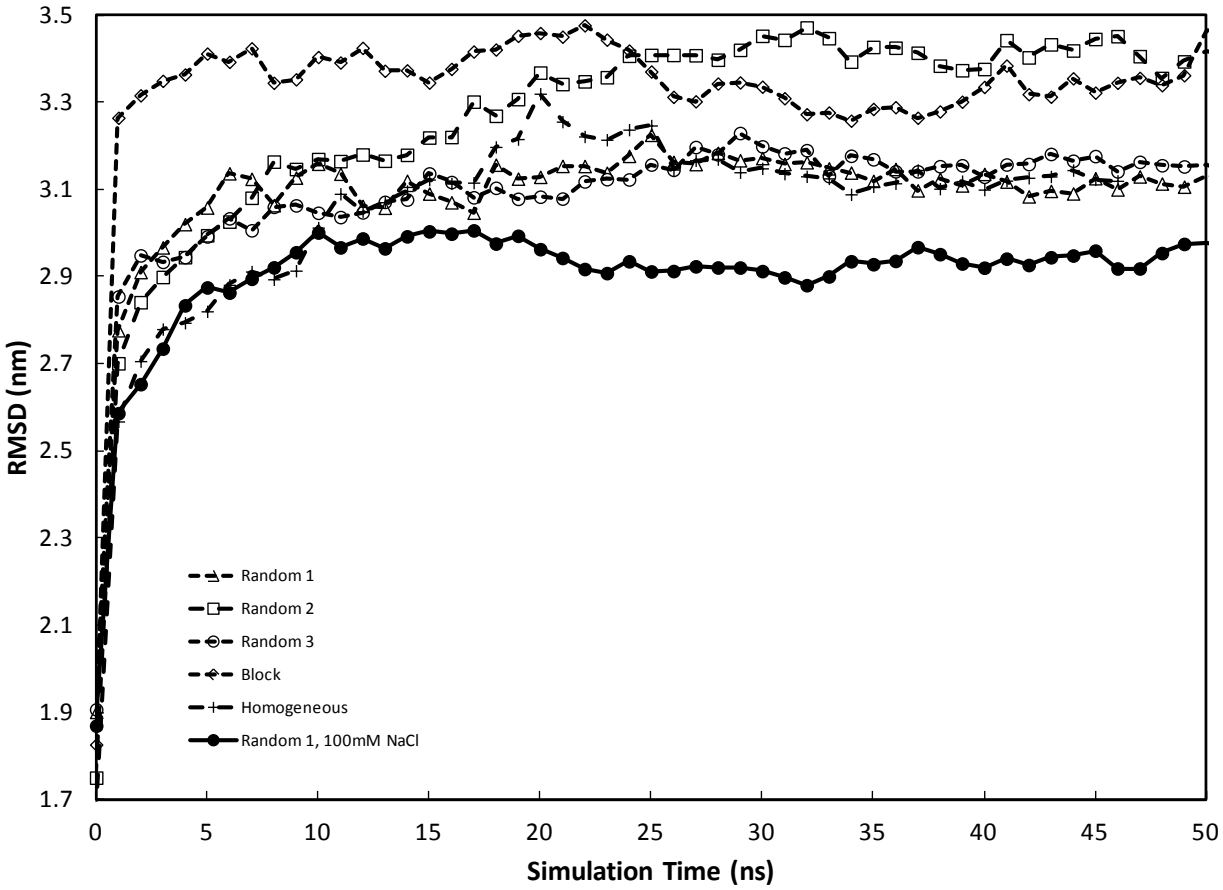

Figure 5. The root mean square deviation (RMSD) plotted against simulation time for each simulation performed, using the backbone α-carbon. This figure indicates that each of the simulations relaxes within ~20 ns. The equilibrium deviation value is between 3 and 3.5 nm for each sequence. The Block and Random 2 configurations plateau at higher values, while the Random 1 + 100mM NaCl system equilibrates to a substantially lower value.

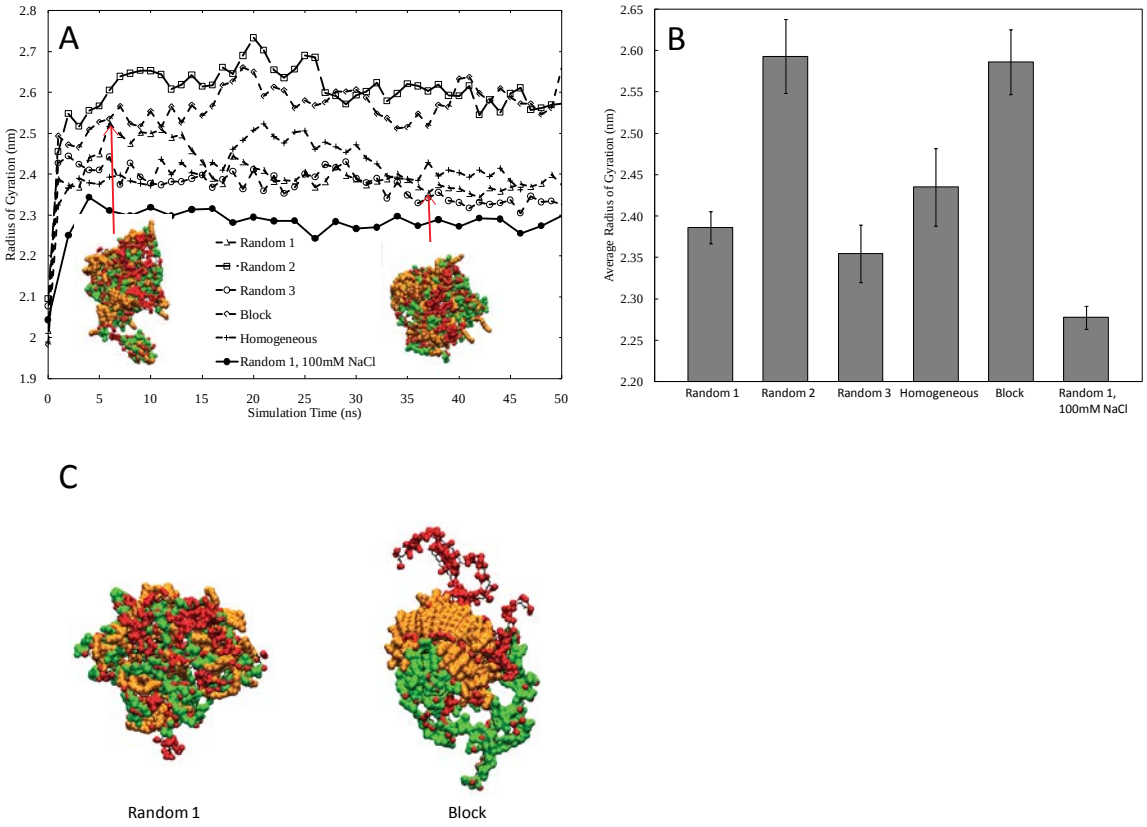

Figure 6. Inset A shows the equilibration of the radius of gyration for each particle over the course of the simulation. The dynamic nature of the shape of amphipol particles is shown from the inlaid snapshots of the Random 1 particle taken at different time points after equilibration. As is shown in this inset, there are periods of time where chains protrude beyond the spherical body (extended) and others where the chains pack together neatly (compressed). B shows the average radius of gyration values after equilibration (20ns) which quantifies changes in size that occur due to polymer side-chain sequence. Inset C illustrates the difference in particle shape due to side-chain organization, by comparing the Random 1 particle (left) and the Block configured particle (right). Red represents carbonyl Oxygens, green represents isopropyl side-chains, and orange represents octyl side-chains.

A

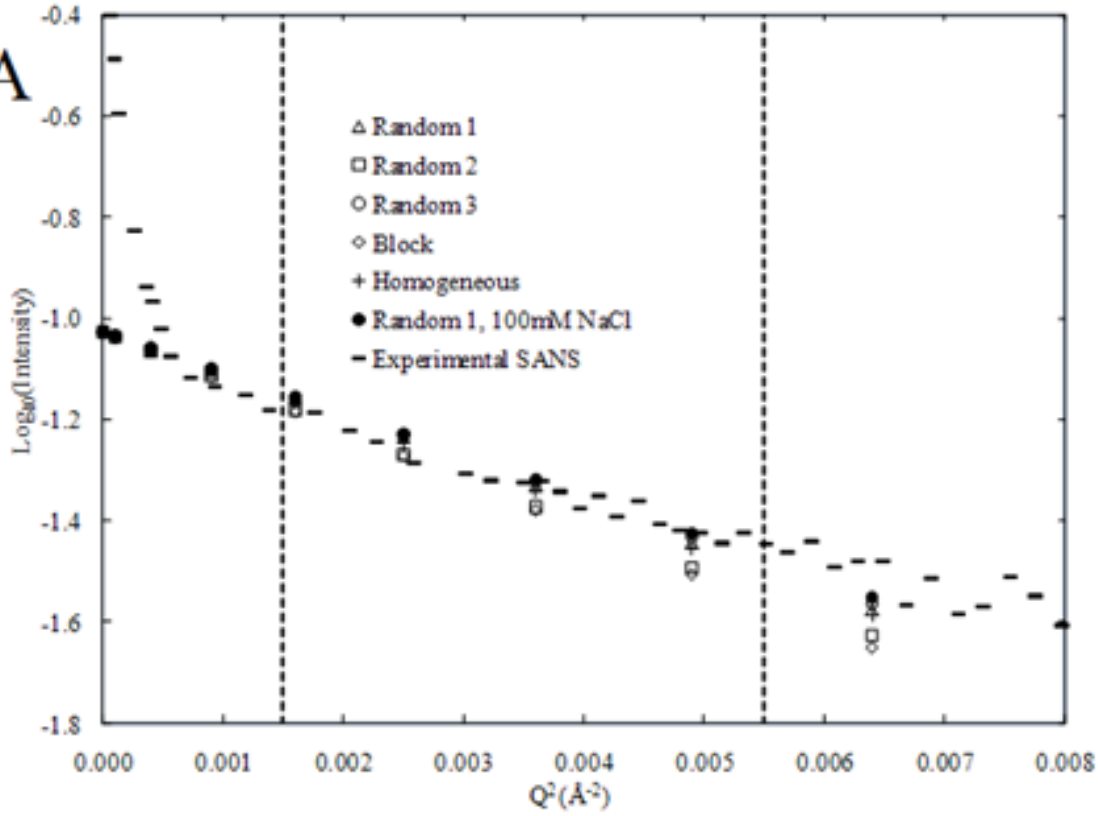

B

Particle	Rg SANS (nm)	Rg CHARMM (nm)
Random 1	2.40	2.39
Random 2	2.58	2.59
Random 3	2.37	2.35
Block	2.60	2.59
Homogeneous	2.46	2.44
Random 1, 100mM NaCl	2.28	2.28

Figure 7. A. Solution behavior of A8-35 particle as probed through simulated small angle neutron scattering (SANS). Simulated SANS data is plotted as the log of intensity versus Q^2 and the radius of gyration is extracted from the slope of the line through the Guinier approximation. Experimentally acquired data by Gohon is overlaid, with the dashed vertical lines enclosing the region used for their radius of gyration analysis (8). Inset B summarizes the radius of gyration values measured directly from simulation and those calculated through simulated SANS analysis.

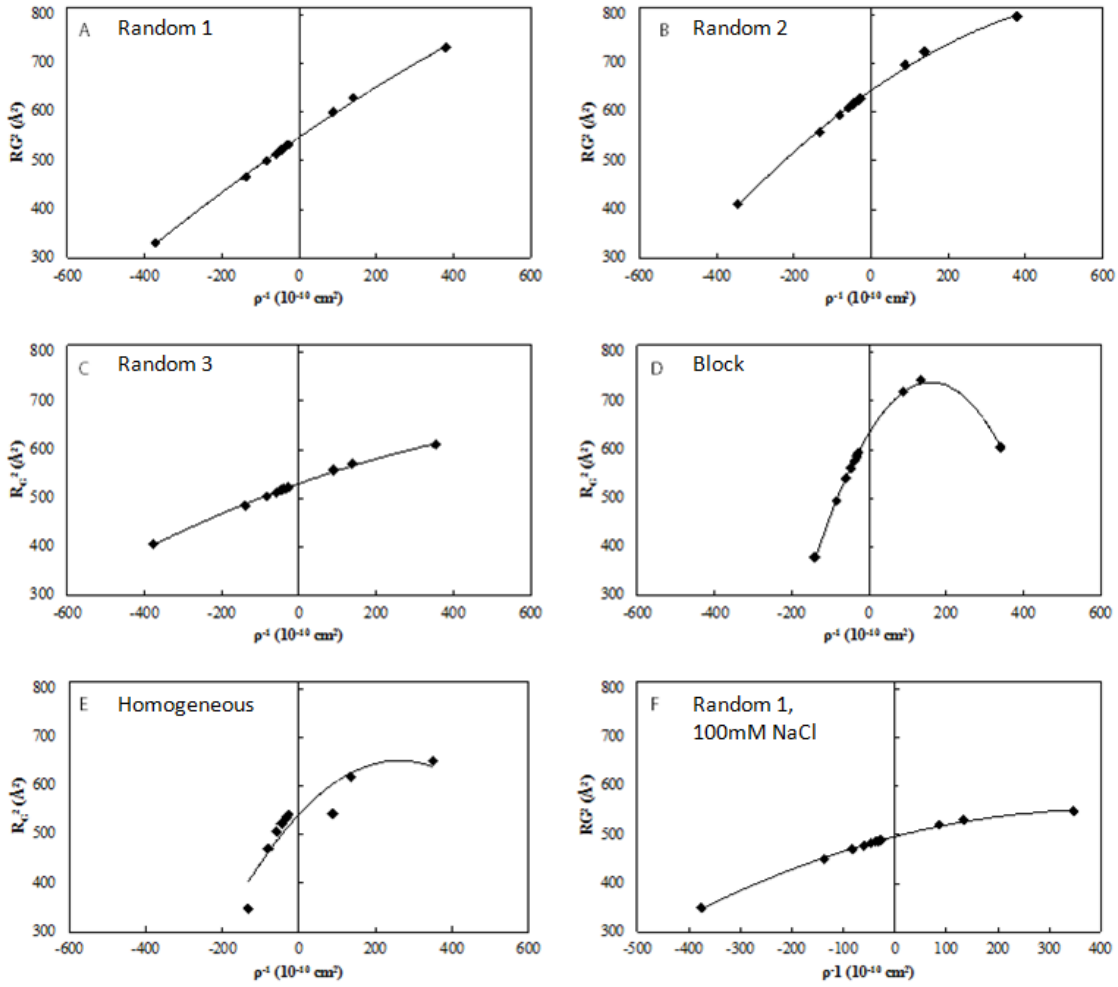

Figure 8. Contrast match point plot with Rg^2 plotted against inverse of contrast for hapol amphipol particles. The intersection of the curve with the ordinate gives a measure of the radius of gyration at infinite contrast.

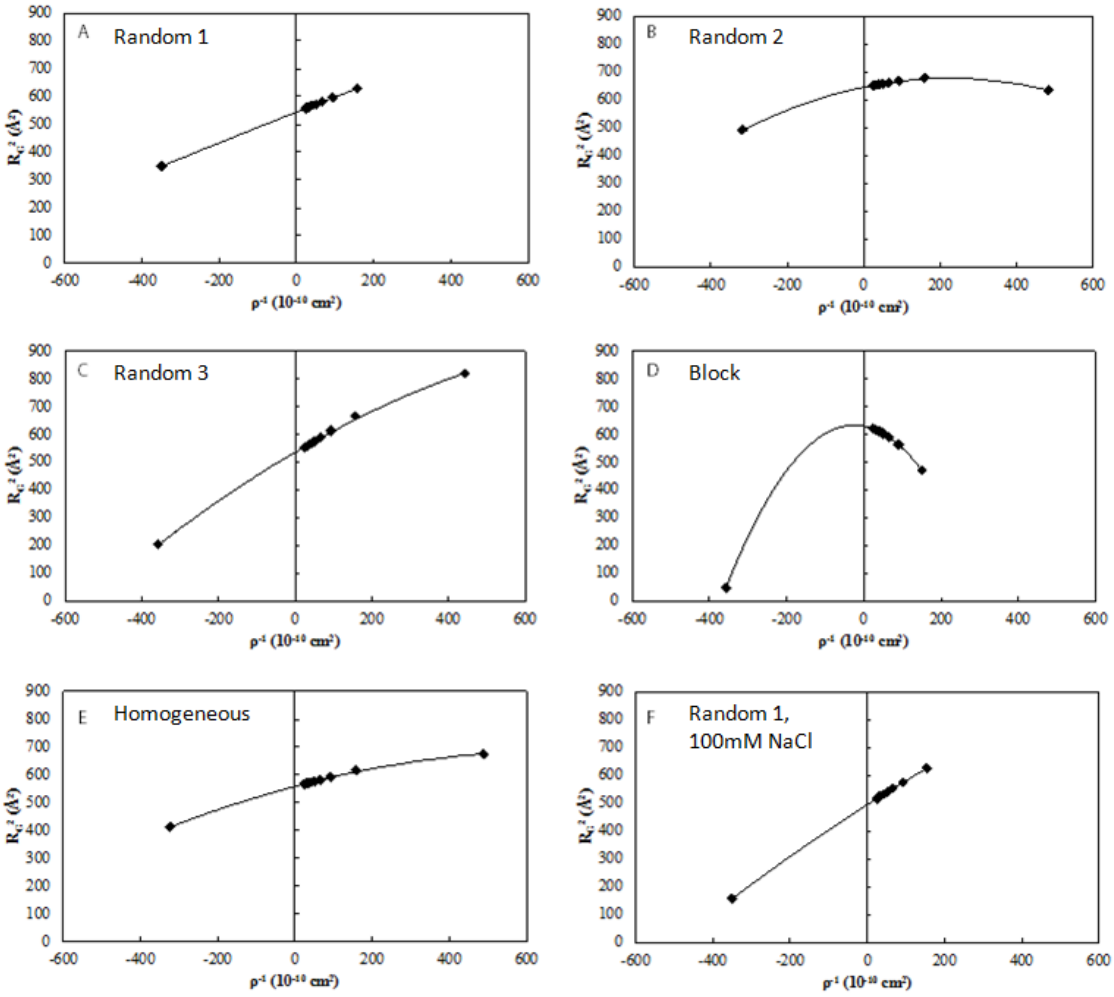

Figure 9. Contrast match point plot with Rg^2 plotted against inverse of contrast for dapol amphipol particles. The intersection of the curve with the ordinate gives a measure of the radius of gyration at infinite contrast.

Table 2. Radius of gyration at infinite contrast for each of the particle models taken from intercept from Figure 8 and 9. Also includes α and β parameters taken from polynomial curve-fits from same figures. The contrast match point taken from Figures A1 and A2 are also listed for each of the particles. That average match points are 0.247±0.003 for hapol and 0.947±0.003 for dapol.

	Hapol				Dapol			
Particle	Rc (nm)	α	β	$^2H_2O/H_2O$ Match Point	Rc (nm)	α	β	$^2H_2O/H_2O$ Match Point
Rand 01	2.34	0.54	0.00013	0.247	2.34	0.50	0.00020	0.947
Rand 02	2.54	0.56	0.00038	0.243	2.54	0.29	0.00064	0.942
Rand 03	2.30	0.28	0.00014	0.248	2.32	0.80	0.00036	0.949
Block	2.52	1.30	0.00405	0.250	2.51	-0.26	0.00529	0.951
Homo	2.36	0.60	0.00011	0.245	2.36	0.37	0.00026	0.942
100mM Na	2.27	0.27	0.00033	0.249	2.24	0.81	0.00049	0.948

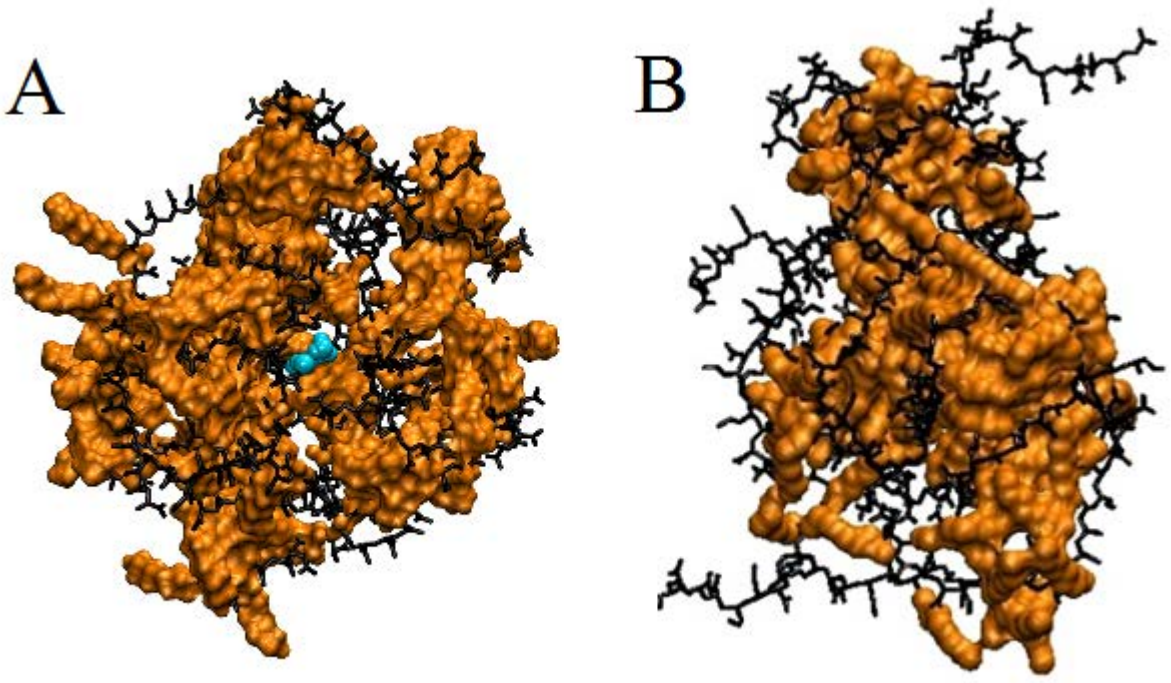

Figure 10. Representative snapshots taken after 50 ns of dynamics, illustrating the polyacrylate backbone in black, the octylamine in orange and (if present) water within 3 Å of the particle center in blue. The Random 1 configuration (A), has water in the particle center, four molecules at this time-point, while the Random 2 configuration (B) effectively excludes water, by spanning the particle center with octylamine side-chains.

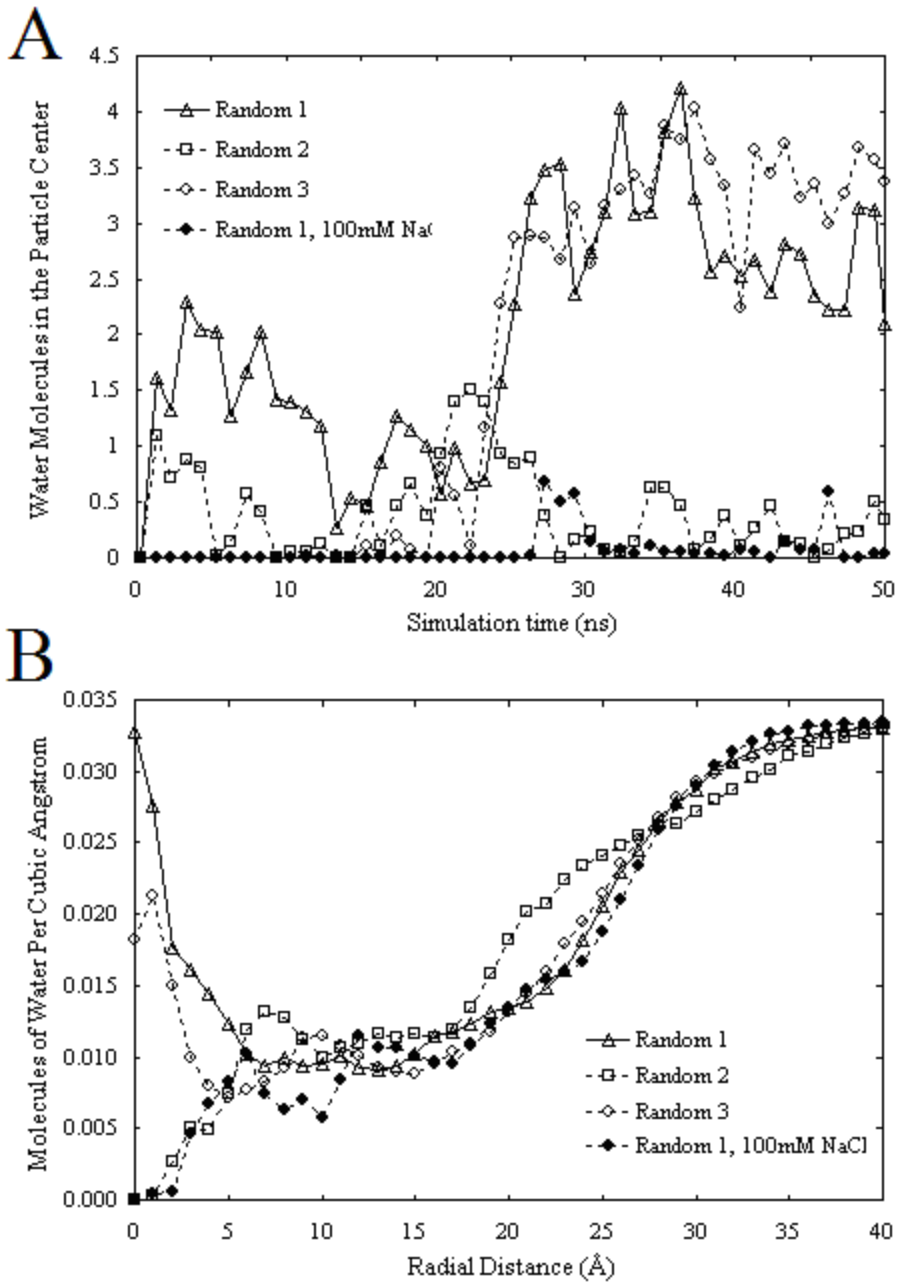

Figure 11. Inset A shows water molecules present at the particle center vs. simulation time. All configurations have no water present in the center at the start of the simulation. These data indicate that water inclusion or exclusion is a dynamic property and does not represent rigid trapping or exclusion of waters. Inset B illustrates water molecules per cubic Angstrom plotted against radial distance from the particles center of mass. Water content is described as the number of water residues present per cubic angstrom. In the Random 1 and Random 3 configurations, we see a concentration of water at the particle core that is near the bulk value. For the Random 2 and Random 1, 100mM NaCl particles, there is little if any water in the particle core. Differences in water content extend out to 9 Å and then behave similarly as they approach the bulk water concentration at high radial position.

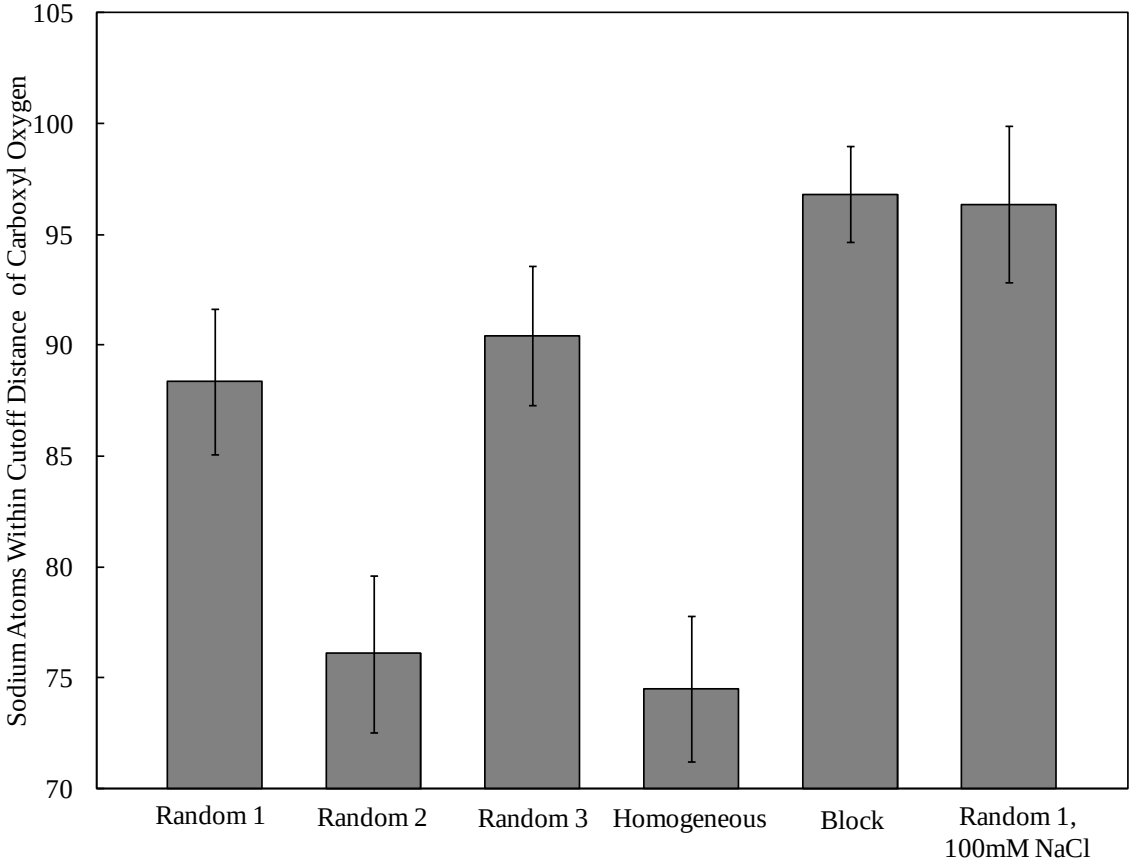

Figure 12. Representation of the average number of sodium ions bound to carbonyl oxygens over the production portion of each simulation. Bound is defined as having position within a 2.5 Å cutoff distance. Error bars indicate deviations over the course of the simulation.

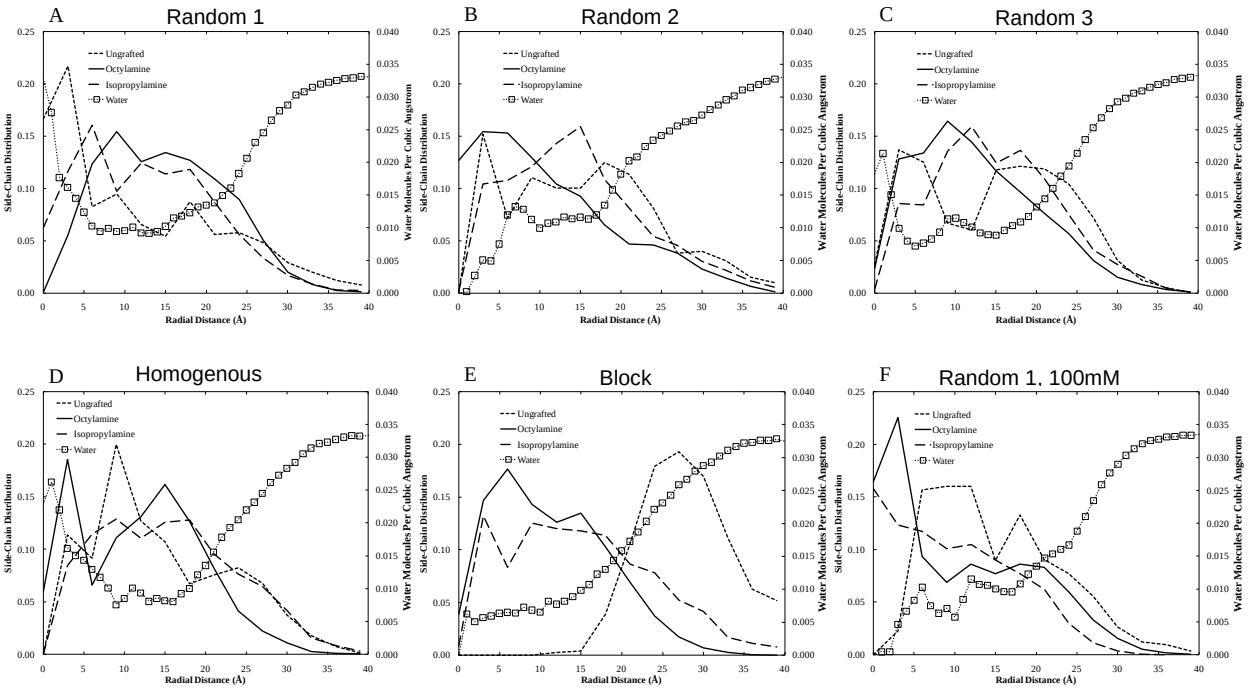

Figure 13. Each inset figure conveys the hydrophilic and hydrophobic atom probability density as a function of radial distance from the mass averaged center of each particle. The water content is overlaid with scale shown on the right ordinate. The differences in organization suggest that these simulations are of sufficient time- and length-scale to observe differences due to polymer sequence and ionic concentration.

References

1. Breyton, C., Tribet, C., Olive, J., Dubacq, J.P. & Popot, J.L. Dimer to monomer conversion of the cytochrome b6 f complex. Causes and consequences. *The Journal of biological chemistry* **272**, 21892-21900 (1997).

2. Sanders, C.R., Kuhn Hoffmann, A., Gray, D.N., Keyes, M.H. & Ellis, C.D. French swimwear for membrane proteins. *Chembiochem : a European journal of chemical biology* **5**, 423-426 (2004).

3. Picard, M. *et al.* Protective and inhibitory effects of various types of amphipols on the Ca2+-ATPase from sarcoplasmic reticulum: a comparative study. *Biochemistry* **45**, 1861-1869 (2006).

4. Wallin, E. & Heijne, G.V. Genome-wide analysis of integral membrane proteins from eubacterial, archaean, and eukaryotic organisms. *Protein Science* **7**, 1029-1038 (1998).

5. Bowie, J.U. Stabilizing membrane proteins. *Current opinion in structural biology* **11**, 397-402 (2001).

6. Popot, J.L. *et al.* Amphipols: polymeric surfactants for membrane biology research. *Cellular and molecular life sciences : CMLS* **60**, 1559-1574 (2003).

7. Laschewsky, A. Molecular Concepts, Self-Organisation and Properties of Polysoaps. *Advances in Polymer Science* **124**, (1995).

8. Gohon, Y. *et al.* Well-defined nanoparticles formed by hydrophobic assembly of a short and polydisperse random terpolymer, amphipol A8-35. *Langmuir : the ACS journal of surfaces and colloids* **22**, 1281-1290 (2006).

9. Breyton, C., Chabaud, E., Chaudier, Y., Pucci, B. & Popot, J.L. Hemifluorinated surfactants: a non-dissociating environment for handling membrane proteins in aqueous solutions? *FEBS letters* **564**, 312-318 (2004).

10. Gohon, Y. *et al.* Partial specific volume and solvent interactions of amphipol A8-35. *Analytical Biochemistry* **334**, 318-334 (2004).

11. Brooks, B.R. *et al.* CHARMM: A program for macromolecular energy, minimization, and dynamics calculations. *Journal of Computational Chemistry* **4**, 187-217 (1983).

12. MacKerell,, a. D. *et al.* All-Atom Empirical Potential for Molecular Modeling and Dynamics Studies of Proteins †. *The Journal of Physical Chemistry B* **102**, 3586-3616 (1998).

13. Schlick, T. Molecular modeling and simulation: an interdisciplinary guide. *95.31.6.178* **21**, (2010).

14. Jorgensen, W.L., Chandrasekhar, J., Madura, J.D., Impey, R.W. & Klein, M.L. Comparison of simple potential functions for simulating liquid water. *The Journal of chemical physics* **79**, 926-935 (1983).

15. Phillips, J.C. *et al.* Scalable molecular dynamics with NAMD. *Journal of Computational Chemistry* **26**, 1781-1802 (2005).

16. Humphrey, W., Dalke, A. & Schulten, K. VMD: Visual molecular dynamics. *Journal of Molecular Graphics* **14**, 33-38 (1996).

17. Perlmutter, J.D. *et al.* All-atom and coarse-grained molecular dynamics simulations of a membrane protein stabilizing polymer. *Langmuir : the ACS journal of surfaces and colloids* **27**, 10523-37 (2011).

18. Svergun, D.I. *et al.* Protein hydration in solution: experimental observation by x-ray and neutron scattering. *Proceedings of the National Academy of Sciences of the United States of America* **95**, 2267-72 (1998).

19. Svergun, D.I. & Koch, M.H.J. Advances in structure analysis using small-angle scattering in solution. *Current opinion in structural biology* **12**, 654-660 (2002).

20. Jacrot, B. & Giuseppe, Z. Determination of Molecular Weight by Neutron Scattering. *Biopolymers* **20**, 2413 (1981).

21. Stuhrmann, H.B., Haas, J., Ibel, K., Koch, M.H. & Crichton, R.R. Low angle neutron scattering of ferritin studied by contrast variation. *Journal of Molecular Biology* **100**, 399-413 (1976).

22. Cantor, C.R. & Schimmel, P.R. *Biophysical chemistry*. (Freeman and Company: New York, 1980).

23. Van Holde, K.E., Johnson, W.C. & Ho, P.S. *Principles of physical biochemistry*. (Prentice Hall: Upper Saddle River, N.J., 1998).

24. Feigin, L.A. & Svergun, D.I. *Structure analysis by small-angle X-ray and neutron scattering*. (Plenum Pr.: New York u.a., 1987).

25. Ibel, K. & Stuhrmann, H.B. Comparison of neutron and X-ray scattering of dilute myoglobin solutions. *Journal of molecular biology* **93**, 255-65 (1975).

26. Tribet, C. *et al.* Thermodynamic characterization of the exchange of detergents and amphipols at the surfaces of integral membrane proteins. *Langmuir : the ACS journal of surfaces and colloids* **25**, 12623-12634 (2009).

27. Zoonens, M., Catoire, L.J., Giusti, F. & Popot, J.L. NMR study of a membrane protein in detergent-free aqueous solution. *Proceedings of the National Academy of Sciences of the United States of America* **102**, 8893-8898 (2005).

28. Hu, Y., Smith, G.L., Richardson, M.F. & McCormick, C.L. Water Soluble Polymers. 74. pH Responsive Microdomains in Labeled n-Octylamide-Substituted Poly(sodium maleate-alt-ethyl vinyl ethers): Synthesis, Steady-State Fluorescence, and Nonradiative Energy Transfer Studies. *Macromolecules* **30**, 3526-3537 (1997).

Appendix

Table A1. CHARMM parameters utilized for each of the particle simulations.

Atom Properties

ATOM	POLARIZABILITY	N (EFF)	RADIUS
H	0.0000	0.0460	0.2245
HA	0.0000	0.0220	1.3200
HT	0.0000	0.0460	0.2245
C	0.0000	0.1100	2.0000
CT1	0.0000	0.0200	2.2750
CT2	0.0000	0.0550	2.1750
CT3	0.0000	0.0800	2.0600
CC	0.0000	0.0700	2.0000
NH1	0.0000	0.2000	1.8500
O	0.0000	0.1200	1.7000
OC	0.0000	0.1200	1.7000
OT	0.0000	0.1521	1.7682
SOD	0.0000	0.0469	1.3638
CLA	0.0000	0.1500	2.2700

Bond Parameters

Bond	Kb	B0
HT - HT	0.0	1.514
CT1 - HA	309.0	1.111
CT1 - C	250.0	1.490
CT2 - HA	309.0	1.111
CT2 - C	250.0	1.490
CT2 - CT2	222.5	1.530
CT3 - HA	322.0	1.111
CT3 - CT1	222.5	1.538
CT3 - CT2	222.5	1.528
CC - CT1	200.0	1.522
CC - CT2	200.0	1.522
NH1 - H	440.0	0.997
NH1 - C	370.0	1.345
NH1 - CT1	320.0	1.430
NH1 - CT2	320.0	1.430
O - C	620.0	1.230
OC - CC	525.0	1.260
OT - HT	450.0	0.957

Bond Angle Parameters

Angle	Kt	T0	Uk	U0
HA - CT2 - HA	35.50	109.00	5.40	1.802
HA - CT3 - HA	35.50	108.40	5.40	1.802
HT - OT - HT	55.00	104.52	0.00	0.000
C - NH1 - H	34.00	123.00	0.00	0.000
C - CT1 - HA	33.00	109.50	30.00	2.163
C - CT2 - HA	33.00	109.50	30.00	2.163
CT1 - NH1 - H	35.00	117.00	0.00	0.000
CT1 - CT2 - HA	33.43	110.10	22.53	2.179
CT1 - CT3 - HA	33.43	110.10	22.53	2.179
CT1 - NH1 - C	50.00	120.00	0.00	0.000
CT2 - NH1 - H	35.00	117.00	0.00	0.000
CT2 - CT1 - HA	34.50	110.10	22.53	2.179
CT2 - CT2 - HA	26.50	110.10	22.53	2.179
CT2 - CT3 - HA	34.60	110.10	22.53	2.179
CT2 - CT1 - C	52.00	108.00	0.00	0.000
CT2 - CT2 - C	52.00	108.00	0.00	0.000
CT2 - NH1 - C	50.00	120.00	0.00	0.000
CT2 - CT2 - CT2	58.35	113.60	11.16	2.561
CT3 - CT1 - HA	34.50	110.10	22.53	2.179
CT3 - CT2 - HA	34.60	110.10	22.53	2.179
CT3 - CT1 - C	52.00	108.00	0.00	0.000
CT3 - CT2 - CT2	58.00	115.00	8.00	2.561
CT3 - CT1 - CT3	53.35	114.00	8.00	2.561
CC - CT1 - HA	33.00	109.50	30.00	2.163
CC - CT2 - HA	33.00	109.50	30.00	2.163
CC - CT1 - CT2	52.00	108.00	0.00	0.000
CC - CT2 - CT2	52.00	108.00	0.00	0.000
CC - CT1 - CT3	52.00	108.00	0.00	0.000
NH1 - CT1 - HA	48.00	108.00	0.00	0.000
NH1 - CT2 - HA	51.50	109.50	0.00	0.000
NH1 - C - CT1	80.00	116.50	0.00	0.000
NH1 - C - CT2	80.00	116.50	0.00	0.000
NH1 - CT2 - CT2	70.00	113.50	0.00	0.000
NH1 - CT1 - CT3	70.00	113.50	0.00	0.000
O - C - CT1	80.00	121.00	0.00	0.000
O - C - CT2	80.00	121.00	0.00	0.000
O - C - NH1	80.00	122.50	0.00	0.000
OC - CC - CT1	40.00	118.00	50.00	2.388
OC - CC - CT2	40.00	118.00	50.00	2.388
OC - CC - OC	100.00	124.00	70.00	2.225

Dihedral Angle Parameters

Torsion	Kp	N	Delta
X - CT2 - CT1 - X	0.20	3	0
X - CT2 - CT2 - X	0.20	3	0
X - CT3 - CT1 - X	0.20	3	0
X - CT3 - CT2 - X	0.16	3	0
X - CC - CT1 - X	0.05	6	180
X - CC - CT2 - X	0.05	6	180
C - NH1 - CT1 - HA	0.00	3	0
C - NH1 - CT2 - HA	0.00	3	0
CT1 - NH1 - C - CT1	1.60	1	0
CT2 - NH1 - C - CT1	1.60	1	0
CT2 - CT2 - CT2 - CT2	0.15	1	0
CT2 - NH1 - C - CT2	1.60	1	0
CT3 - CT2 - CT2 - CT2	0.15	1	0
H - NH1 - CT1 - HA	0.00	1	0
H - NH1 - CT2 - HA	0.00	3	0
H - NH1 - C - CT1	2.50	2	180
H - NH1 - C - CT2	2.50	2	180
H - NH1 - CT2 - CT2	0.00	1	0
C - NH1 - CT2 - CT2	1.80	1	0
H - NH1 - CT1 - CT3	0.00	1	0
C - NH1 - CT1 - CT3	1.80	1	0
HA - CT1 - C - NH1	0.00	1	0
HA - CT2 - C - NH1	0.00	3	0
CT2 - CT1 - C - NH1	0.00	1	0
CT2 - CT2 - C - NH1	0.00	1	0
CT3 - CT1 - C - NH1	0.00	1	0
H - NH1 - C - O	2.50	2	180
HA - CT1 - C - O	0.00	1	0
HA - CT2 - C - O	0.00	3	180
CT1 - NH1 - C - O	2.50	2	180
CT2 - CT1 - C - O	1.40	1	0
CT2 - CT2 - C - O	1.40	1	0
CT2 - NH1 - C - O	2.50	2	180
CT3 - CT1 - C - O	1.40	1	0

Improper Torsion Parameters

Torsion	Kp	N	Delta
NH1 - X - X - H	20	0	0
O - X - X - C	120	0	0
OC - X - X - CC	96	0	0

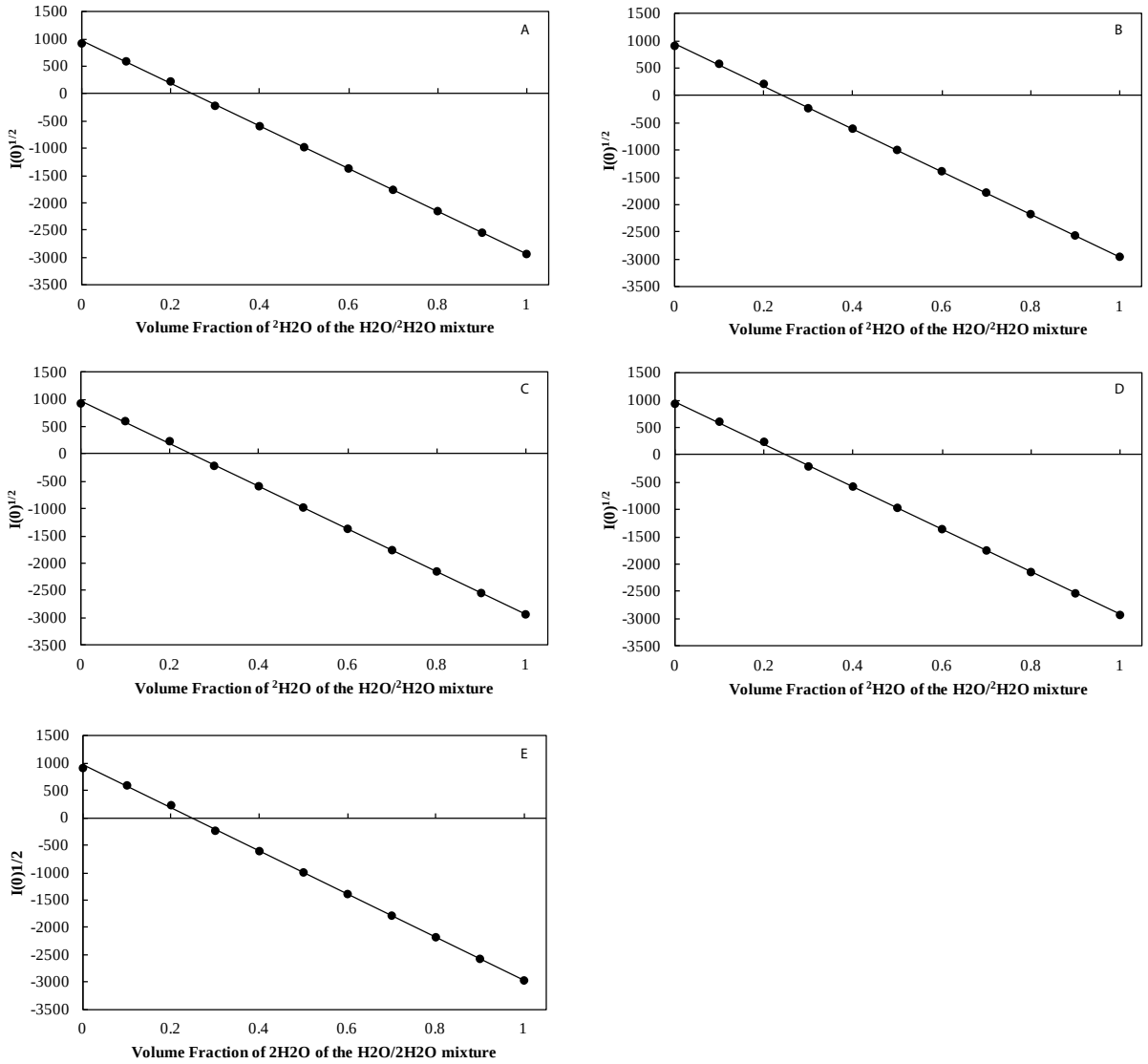

Figure A1. Square root of zero-angle intensity plotted against D2O concentration for each hapol model. Intersection with abscissa indicates contrast match point. A-E represent Random 1, Random 2, Random 3, Block, Homogeneous, and Random 1 with 100mM NaCl respectively.

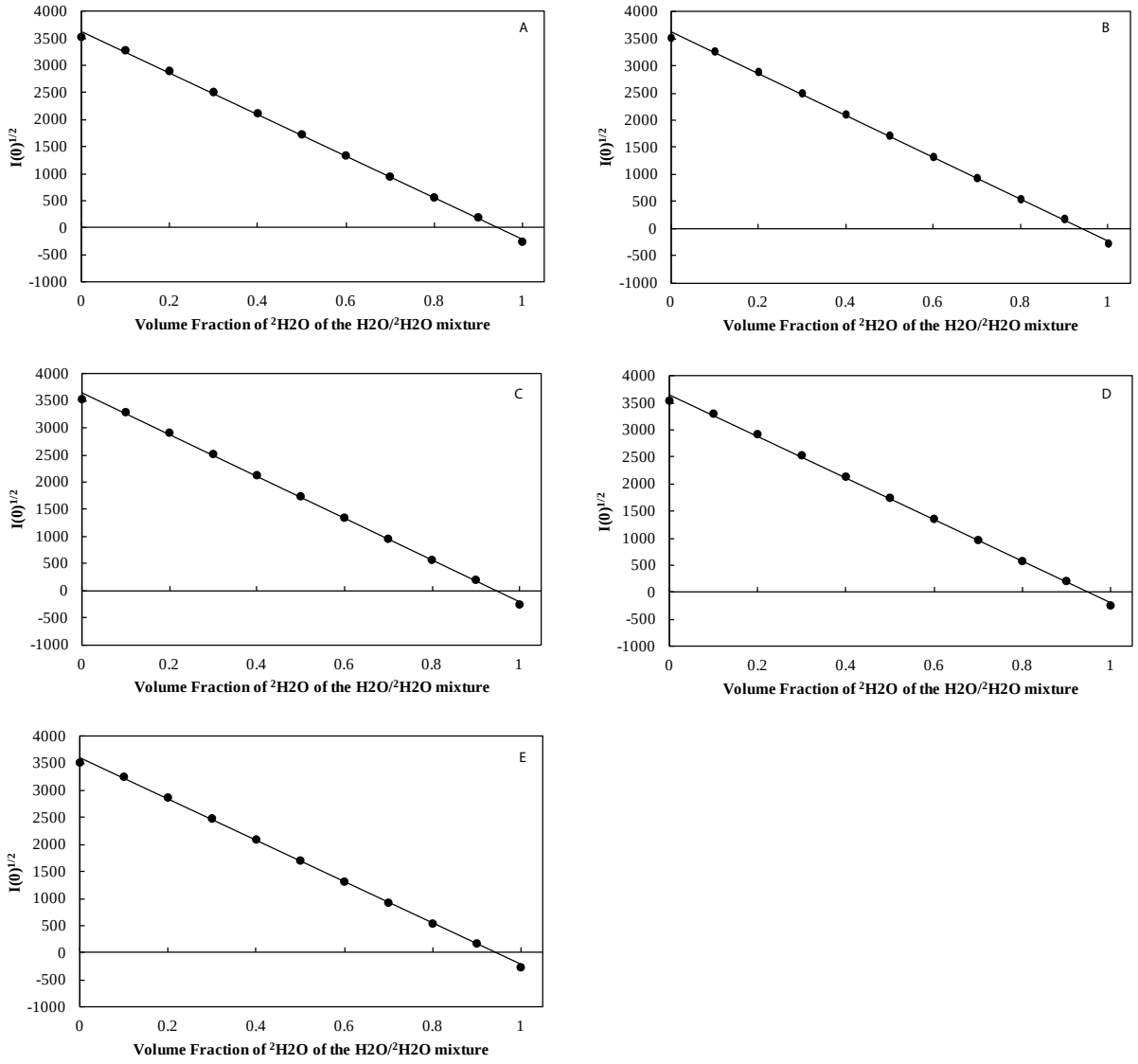

Figure A2. Square root of zero-angle intensity plotted against D2O concentration for each dapol model. Intersection with abscissa indicates contrast match point. A-E represent Random 1, Random 2, Random 3, Block, Homogeneous, and Random 1 with 100mM NaCl respectively.